Aerodynamic Performance Improvement of a Wing Model Using an Array of Slotted Synthetic Jets

Pramod Salunkhe[1*], Yanhua Wu[2], Hui Tang[3],

[1]Department of Aeronautical and Automobile Engineering, Manipal Institute of Technology, Karnataka, India

[2]School of Mechanical & Aerospace Engineering, Nanyang Technological University, Singapore

[3]Research Center for Fluid Structure Interactions, Department of Mechanical Engineering, Hong Kong Polytechnic University, Hong Kong

*pramod.salunkhe@manipal.edu

Abstract

The present work deals with the improvement in aerodynamic performance of a NACA0025 wing model using an array of slotted synthetic jets (SJs). A novel synthetic jet actuator was designed and located at 30% chord from the leading edge. Time-Resolved Particle Image Velocimetry (TR-PIV), force balance, static pressure distribution and hot wire measurements were carried out in a subsonic wind-tunnel to assess the performance enhancement due to the slotted SJ array. Initially, the SJ velocity was measured in quiescent flow condition at different actuation frequencies and amplifier voltages. Actuation at 1000 Hz and 200 V resulted in the highest blowing velocity of 10.5 m/s. Experiments were performed at various actuation frequencies, namely, 200, 600 and 1000 Hz. It was observed that, actuation at 1000 Hz led to the highest increase in lift coefficient by 35.6% and reduction in average drag coefficient by 33%. TR-PIV measurements showed flow separation with flow reversal in the baseline case. After switching on the SJ array at 1000 Hz, the flow separation was completely eliminated. The momentum transfer from the high energy primary flow to the retarding boundary layer flow and actuation of SJ in a particular frequency range was observed to be the mechanisms for the flow separation control. Subsequently, FFT power spectra of hot wire data were computed from 40%

to 80% of the chord. The FFT power spectra showed the successful stabilization of the flow field at the actuation of 1000 Hz.

Keywords: *Active flow control, synthetic jet, aerodynamic performance, lift-to-drag ratio*

1 Introduction

Active flow control (AFC) is still a hot topic in past few decades. One of the promising AFC means is the use of synthetic jet (SJ). Oscillation of a piezoelectric diaphragm causes successive suction and blowing in the surrounding fluid medium, forming a vortex ring which propagates away from the actuation surface. A train of these vortices then forms a SJ. Although it is a local flow phenomenon, if deployed properly, SJ can play a significant role in altering the global behavior of the flow, such as in flow separation control [1-5], heat transfer enhancement [6-9], fluid mixing [10-12] etc. As for the flow separation control, Tang et al. [13] described three mechanisms of flow separation control over a wing model, viz. i. direct momentum injection into the free-stream flow by blowing; ii. momentum exchange between the free-stream flow and the retarding boundary layer flow due to SJ vortex structures; and iii. oscillation of piezoelectric diaphragm in a certain frequency range that affects the instability of the shear layer. Amitay et al. [14] reported that the best control effects can be obtained if SJ actuators are placed close to the separation point. The lift and drag coefficients were increased by 100% and 45%, respectively at a chord Reynolds number of 7.25×10^5. At the reduced frequency $F^+ > 4$, the lift-to-pressure-drag ratio was found to be reduced, whereas, at $F^+ \geq 10$, this ratio was significantly increased. Glezer et al. [15] investigated the effect of low and high frequency actuation on an unconventional airfoil. It was reported that the high-frequency actuation leads to a thin and stable boundary layer that help improve the aerodynamic performance. The low-frequency actuation was found to be less effective as it gives a strong coupling between the actuation frequency and the global

instabilities. This coupling was not observed at high actuation frequency. In contrast to the above findings, Frank and Colonius [16] in their computational investigations reported that the low-frequency actuation in the order of natural shedding frequency is the most effective in decreasing the separation region as compared to high-frequency actuation. This was attributed to the formation of large vortical structures that help reattach the flow. The high-frequency actuation forms small vortices that dissipate rapidly. Timor et al. [17] carried out experimental studies on a NACA 0018 airfoil over a range of Re = 1.6 to 3 x 10^5 using an array of 14 SJ actuators placed at 88% of the chord. The lift coefficient was found to be significantly increased after switching on all the SJs. The rolling moment was substantially increased when only the SJs on the half-span of the wing were actuated. Sefcovic and Smith [18] located an array of SJ actuators at the leading and trailing edge of a NACA 65_2 -215 airfoil. It was observed that the leading-edge actuators help control the flow separation and increase the maximum lift coefficient. The trailing-edge actuators were found to enhance the lift-to-drag ratio below the stall angle of attack.

Traub et al. [19] carried out experimental studies on a NACA 0015 airfoil by ramping it from 0° to 27°. At higher angles of attack the onset of stall was found to be delayed after switching on the SJ actuators, which can be attributed to the direct momentum addition. Kordik and Travnicek [20] performed optimization of nozzle diameter of a SJ actuator for nine nozzle geometries, ten power levels and two transducers, i.e. loudspeakers. For the two transducers, the optimal nozzle diameters was found to be in the range of 11.1 ~ 20.4 mm and 8.7 ~ 14.2 mm, respectively. Excellent agreement was found between the experimental results and the lumped element modeling. The highest energetic efficiency of 15% was reported.

Hong [21] carried out experimental studies to control the laminar flow separation over a flat plate with a fairing. The adverse pressure gradient was formed by changing the angle of the fairing. The SJ actuator was driven by a low voltage of ±7.5 V. A better resistance to the laminar

flow separation was observed at a lower effective forcing frequency of 100 Hz. It was reported that the SJ actuator triggers and amplifies the T-S instability which helps control the K-H instability. Similarly, Lee et al. [22] also observed that the actuation at lower frequencies is more effective than that at higher frequencies. It was noticed that the effectiveness of a SJ actuator depends strongly on the forcing frequency rather than forcing voltage. Subsequently, Amitay and Glezer [23] performed in-depth investigations on aerodynamics of a stalled airfoil by changing the non-dimensional actuation frequency, F^+, from the order of natural shedding frequency, O(1), to substantially higher values, i.e. O(10). It was reported that at $F^+ \sim O(1)$ the formation of large-scale vortical structures causes unsteady reattachment, whereas actuation at $F^+ \sim O(10)$ results in a complete flow attachment with absence of large-scale vortical structures. The lift-to-drag ratio was found to be reduced with the increase in actuation frequency above the natural shedding frequency.

Salunkhe et al [24] analyzed the effectiveness of a SJ array on airfoil LS(1)-0421MOD using three-dimensional Tomographic PIV measurements. The highest effectiveness of the SJ array was observed at 180° phase angle which corresponds to the instant when the maximum blowing occurs. The improvement in wing performance due to the SJ array was attributed to the exchange of momentum between the SJ-induced vortices propagating downstream and the retarding boundary layer flow. Rimasauskiene et al. [25] optimized the design of a SJ actuator for the highest possible jet velocity. The parametric study was carried out by varying the number of orifices (one and three) and cavity height (0.5 and 1.5 mm). The highest jet velocity of 25 m/s was obtained for the configuration of a single orifice and cavity height of 0.5 mm.

Our previous SJ actuators had a low SJ velocity of only about 7.5 m/s resulting in a lower momentum coefficient of 4.2×10^{-5}. This provided impetus to design a novel SJ actuator that can impart higher SJ velocity and hence higher momentum coefficient with reduced number of

piezoelectric diaphragms. Reduction in the number of piezoelectric diaphragms substantially reduces the power consumption. Another objective of the present work is to estimate the performance improvement of the wing by varying the SJ actuation frequency. The wing performance is assessed through different measurements, namely, the Time Resolved-Particle Image Velocimetry (TR-PIV), force balance, static pressure distribution, hot wire etc.

2 Experimental Set-up and Instrumentation

The experiments were carried out in a subsonic wind tunnel of size 2 m (L) × 0.78 m (W) × 0.72 m (H) on a NACA 0025 wing model with a realistic free-stream flow speed of 10 m/s. This flow speed corresponds to a Reynold number of 1.5×10^5. The wing has a chord of 0.24 m and a span of 0.4 m. A new SJ actuator was designed as depicted in Fig. 1(a). It comprises of two piezoelectric diaphragms (7BB-27-4LO from Murata Manufacturing Co. Ltd., Japan) separated by a cavity height of 8 mm. The cavity volume of the present SJ actuator is only about 6.96×10^{-6} m^3. The SJ is generated through a rectangular slot of 0.5 mm (W) × 12 mm (L) × 2 mm (H) that is cut on the suction surface of the wing model (as shown in Fig. 1(b)). The present SJ actuator is different from our previous SJ actuator, where the latter uses a larger cavity (13.8×10^{-6} m^3) and an orifice of five circular holes of 1 mm diameter [13]. The slotted construction for the present actuator increases the mass flow rate whereas small cavity volume help increase the SJ velocity. Eleven such SJ actuators were installed inside the wing model at 30% of the chord and evenly distributed in the spanwise direction, as shown in Fig. 1(b). In the present work, in total 22 piezoelectric diaphragms were used as against 40 diaphragms in our previous work [13]. The center-to-center distance between the two successive SJ slots is 35 mm. These SJ actuators were driven in phase using two power amplifiers (EPA-104 from Piezo Systems Inc., USA). A function generator was used to generate a sinusoidal waveform at different frequencies.

A six-component force balance system (Nano17 from ATI Industrial Automation, USA) was used to measure the axial and normal forces acting on the wing. These forces were further resolved to obtain the lift and drag forces. The jet velocity generated by the SJ array is measured using a hot-wire anemometer (Miniature CTA 54T30 from Dantec Dynamics A/S, Denmark). A one-dimensional hot-wire probe, 55P16, was used for this purpose. A NI PCI 6040E data acquisition system was used to acquire the data with a sampling frequency of 10 kHz and 1000 number of samples. Before carrying out measurements the hot-wire probe was calibrated based on the King's law.

A 16-channel, 16-bit digital pressure scanner (DSA 3217 from Scanivalve Corp., USA) was used to measure the static pressure distribution from 22% to 78% of the chord. The first two static pressure ports were located at 22% and 39% of the chord, respectively. The space between these two ports was utilized for the installation of actuators. After the second pressure port, all other ports were arranged with a uniform spacing of 3% of the chord.

A Time-Resolved Particle Image Velocimetry (TR-PIV) system was used to determine two-dimensional velocity components over the suction surface of the wing model. A schematic of the TR-PIV system is shown in Fig. 2. A double pulsed Nd:YLF laser beam (Litron LDY 300) of energy 14 mJ/pulse and wavelength 527 nm was issued from a laser head and passed through four mirrors and subsequently two spherical lenses and a cylindrical lens to form a laser sheet of 1 mm thickness, as shown in Fig. 2. The laser sheet was located at the center of the third SJ actuator slot from left side of the wing, as depicted in Fig. 3. To capture more flow-field information along the chordwise direction, two sets of TR-PIV measurements were conducted. In the first set, the field of view lies between 26% and 59% of the chord, whereas in the second set it is between 59% and 92% of the chord. In the first set, the laser sheet starts from a location 10 mm upstream of the SJ array (i.e. 26% of the chord). For each set of measurements, the maximum

length of field of view in the chordwise direction was 80 mm. The total field of view was then 160 mm x 85 mm.

A Laskin nozzle was used to seed the air flow with olive oil particles of size around 1-2 µm. A CCD camera of 16 bit and 1024x1024 resolution captured the illuminated flow-field. The camera lens has a focal length of 60 mm and the smallest f number of 2.8. The repetition rate was maintained at 1000 Hz. The time delay between the two laser pulses was set at 85 µs. Data acquisition and analysis were performed using the TSI Insight 4G software. The velocity field was computed using two-dimensional cross-correlation of reconstructed particles. The interrogation area of 24 × 24 pixels was chosen to calculate the velocity vectors, such that 84 × 84 vectors with a vector grid spacing of 1.04 mm were obtained in each velocity field. Bad velocity vectors were identified and replaced using a local median filter in the neighborhood size of 3 × 3. A single run consists of 1200 velocity vector files. First, the time average of each run was computed. Subsequently, the time average of above computed ten time averaged runs was then computed.

The hot wire probe has a velocity measurement range of 0.2 ~ 500 m/s and the uncertainty in velocity measurement is about 0.8%. The hot wire calibration using a pitot-static tube constitutes a major source of uncertainty. The calibration error was determined by taking the standard deviation of the velocity data. The pressure scanner has a measurement range of ±5 inch H_2O differential pressure. The measurement uncertainty in static pressure is ±0.05% of the full scale. The measurement range and resolution of the force sensor is 17 N and 0.003 N, respectively. The uncertainties in lift and drag coefficients were determined from the Taylor series expansion. These uncertainties were found to be 0.2% and 0.5% of the full scale output, respectively. The uncertainty in velocity measurement by the TR-PIV was computed using Taylor series expansion by considering uncertainties in PIV cross-correlation, calibration and timing. The cross-

correlation uncertainty was determined from the ratio of first to second highest peak of the correlation [26]. The calibration uncertainty consisted of uncertainty in physical length of ruler, image plane length, image distortion due to aberrations and distance between the calibration scale and the camera lens. These values were taken as 10 μm, 0.1% of image plane length, 0.5% of image plane length and 0.05% of the distance between the calibration scale and the lens, respectively. The timing uncertainty comprised of uncertainty in laser pulse timing and delay generator. Those values were taken as 1 ns and 1.5 ns, respectively. The overall uncertainty in velocity measurement was about 2.51% of the maximum velocity. The estimation of all above uncertainties using different instruments was carried out based on the guidelines provided by Moffat [27], Holman [28] and Lazar et al. [29].

3 Results and Discussion

The SJ array was driven with 200 V peak voltage at different frequencies, namely, 200, 600 and 1000 Hz. The corresponding reduced frequencies, defined as $F^+ = fc/U_\infty$, were 4.8, 14.4 and 24, respectively, where, f is actuation frequency, c is chord and U_∞ is free-stream velocity. The strength of a vortex depends on the Stokes number which is the ratio of unsteady force to the viscous force, i.e., the vortex rolls up if the Stokes number is higher than about 10 [30]. In the present study the Stokes number at 200 Hz, 600 Hz and 1000 Hz was found to be 7.5, 15.2 and 19.6, respectively. The momentum coefficient represents the momentum transferred by the SJ array to surrounding flow, evaluated using $C_\mu = nAU_j^2/bcU_\infty^2$, for the SJ array actuated at 200, 600 and 1000 Hz was 2.4×10^{-6}, 1.6×10^{-4} and 7.8×10^{-4}, respectively, where n is number of actuators, b is wing span, U_j is jet velocity at the exit of SJ slot and A is area of SJ slot.

The SJ velocity was measured using a hot-wire probe. The probe was placed at the slot center aligned with the axis of the slot. Figure 4 shows the variation of SJ velocity against the actuation frequency at three applied excitation voltages, namely, 100, 150 and 200 V. It can be seen that, for a given excitation voltage, the SJ velocity increases with frequency until it reaches a peak at 1 kHz. Amongst all the excitation voltages, the highest SJ velocity of 10.5 m/s was obtained at 200 V. The present piezoelectric diaphragm's resonance frequency is 4.6 kHz. This resonance frequency is significantly higher than the 1 kHz frequency, indicating that the 1 kHz frequency is the Helmholtz frequency of the actuator.

The force balance measurements were carried out to determine the lift and drag coefficients. Figure 5(a) shows the variation in lift coefficient against various angles of attack (AOA) at different actuation frequencies. It is observed that up to 10° AOA, the variation in lift coefficient is marginal for both, uncontrolled (henceforth referred as baseline case) and controlled cases. For the baseline case, the lift coefficient increases gradually up to 18° AOA and drops abruptly representing the onset of stall. The actuation at 600 Hz shows the onset of stall after 20° AOA. However, the reduction in lift coefficient is very mild between 20° to 24° AOA. The gentle reduction in lift coefficient is attributed to the increased resistance to the flow separation due to increase in momentum coefficient corresponding to the actuation at 600 Hz. Beyond 24° AOA, the increased adverse pressure gradient prevails the resistance to flow separation and causes a sharp reduction in lift coefficient. Surprisingly, after switching on the SJ array at 1000 Hz, the lift coefficient is gradually increased and has not entered the stall mode. This shows that the actuation at 1000 Hz is significantly effective for the flow separation control. The enhancement in lift at 200, 600 and 1000 Hz over the baseline case was found to be 1.7%, 20.5% and 35.6%, respectively. Donovan et al. [31] reported the maximum enhancement in lift coefficient by 29% by using SJ actuators on NACA 0012 airfoil, whereas Seifert et al. [32] observed maximum 22%

lift improvement on Pr8-40-SE airfoil. The highest improvement in lift coefficient in our previous studies was about 27.4% [13]. The comparison of above values of improvements in lift coefficient shows the superiority of our SJ actuator design. The highest improvement at 1000 Hz in the present work can be attributed to the higher Stokes number of 19.6 that leads to vortex structures with more coherence and hence deeper penetration into the primary flow, and higher SJ velocity of 10.5 m/s that results in a high momentum coefficient of 7.8×10^{-4}. Amongst all actuation cases, SJ actuation at 200 Hz resulted in negligible improvement in lift due to the significantly low momentum coefficient of 2.4×10^{-6} and Stokes number of only 7.5.

Figure 5(b) shows the variation in drag coefficient against AOA at different actuation frequencies. It is observed that for the baseline case, the drag coefficient increases steadily until 18° AOA. After the onset of flow separation, the drag coefficient shoots up abruptly due to the sharp rise in pressure drag. Among all the cases, the lowest reduction in average drag coefficient of 33% is observed for the actuation at 1000 Hz as the wing has not experienced the onset of stall. The actuation at 600 Hz resulted in the average drag coefficient of 25%, whereas, negligible effect was observed on the average drag coefficient for the actuation at 200 Hz.

The flow-field was analyzed at an angle of attack of 18^{o} using the TR-PIV measurements. Figure 6 presents the time-averaged vorticity contours superimposed with velocity vectors for the baseline case. The vortex structures were identified using the λ_{ci} method. According to this method, a vortex is identified if the absolute value of imaginary part of complex eigen value of a velocity gradient tensor is nonzero. Previously, Salunkhe et al. [24] and Lee and Wu [33] used the λ_{ci} method to identify the vortical structures on LS(1)-0421MOD airfoil and on a horizontal axis wind turbine blade, respectively. To show the dominant vorticity contours, the λ_{ci} value was cut-off below 20 and above 400. At high AOA the pressure substantially increases along the

suction surface of the wing. It is observed that the boundary layer flow does not have sufficient momentum to prevail the increased pressure gradient, as shown by flow reversal in Fig. 6. A shear layer initiates near 30% chord from the leading edge (LE) and move towards the trailing edge (TE). The shear layer trajectory grows substantially and moves away from the wing surface along its path.

Figure 7 depicts the time-averaged vorticity contours for the controlled case with SJ actuation at 1000 Hz and 200 V. In contrast to Fig. 6, the flow is completely attached in this case. The SJ actuation causes direct momentum addition to the retarding boundary layer flow resulting in successful elimination of flow separation. The shear layer trajectory was almost vanished when the actuation is switched on. A train of vorticity contours close to the wing surface was clearly observed in Fig. 7. These vorticity contours are responsible for momentum exchange from the high energy primary flow to the low energy boundary layer flow. Tang et al. [13] has reported three flow separation control mechanisms that causes partial or complete flow re-attachment. These mechanisms are described in section 1. Out of these three mechanisms, the second and third mechanisms are responsible for the significant improvement in flow-field in the present case. The second flow control mechanism deals with the momentum transfer from outer high momentum fluid to the inner low energy boundary layer flow through SJ vortices. The third mechanism refers to the oscillation of SJ in a particular frequency range affecting the instability of the separated shear layer. The second mechanism works at local level, whereas, third one works at global level. The result of these two mechanisms is the successful stabilization of the flow-field over the wing model, as evident from Fig. 7.

Figure 8 shows variation in the shape factor *H*, defined as the ratio of the displacement to momentum thickness for a boundary layer, along the chord for the controlled case with SJ actuation at 1000 Hz and 200 V. From the TR-PIV data, the displacement thickness and momentum thickness were determined in wall-normal direction at different locations along the chord. The shape factor is then computed by taking ratio of displacement thickness and the momentum thickness. The shape factor reflects the type of a boundary layer, a value lower than 2.5 indicates a turbulent boundary layer. As compared to the laminar boundary layer, the turbulent boundary layer offers more resistance to the flow separation. Therefore, in the vicinity of flow separation, a turbulent boundary layer is preferred. Without SJ actuation, the flow over the wing model is separated. The shape factor is not referred in separated flows, hence, in Fig. 8 it is not shown for the baseline case. After actuation of the SJ array, the shape factor is found to be significantly reduced to below 2.5, representing the transition to the turbulent boundary layer. It is also observed that the shape factor gradually increases from the LE to the TE. This indicates that the resistance to the flow separation reduces along the chord.

The Fast Fourier Transform (FFT) power spectra was also computed based on the hot wire measurements. The hot wire probe was placed 8 mm above the suction surface and traversed from 40% to 80% of the chord with a uniform spacing of 8% of the chord. The FFT power spectra shows the variation in power of a given signal against different frequencies. The power of a signal shoots up after the occurrence of a disturbance or stall precursor. In order to prevent or delay the onset of flow separation, damping of these flow disturbances is very important. Figure 9 shows the FFT power spectra for the baseline and various controlled cases. Figure 9(a)-(c) shows a significant spike in SJ controlled cases which corresponds to the SJ actuation frequency. This spike was not observed when the hot wire probe was traversed beyond 56% of the chord which is

far away from the actuator location. It was observed that the SJ actuation at 600 Hz and 1000 Hz are significantly effective in damping out the disturbances. Figure 9(a) shows that up to 1000 Hz frequency, the mean FFT power spectra for the baseline case lies in the range of -5 dB to -30 dB. It reduces in the range of -30 dB to -40 dB for the actuation at 1000 Hz. It was also found that the effectiveness of the SJ actuation reduces from the leading edge towards the trailing edge as can be seen in subplots Fig. 9(a)-(f). Actuation at 200 Hz was found to be ineffective as compared to other actuation cases. The above results indicate that the present SJ array is very effective in stabilizing the flow-field at the actuation frequencies of 600 Hz and 1000 Hz. The stabilization of flow-field is associated with reduction in strength of vortex structures that are generated and evolved due to the flow separation. The effectiveness of control at the actuation frequency of 1000 Hz is evident from the TR-PIV measurements (Fig. 8) and also supported by the force balance measurements (Fig. 5).

The static pressure was measured along the chord. Figure 10 presents the pressure coefficient distribution i.e. the ratio of time-averaged static pressure and dynamic pressure, from 20% to nearly 80% of the chord. For the baseline case and weak actuation at 200 Hz, the static pressure distribution was almost constant throughout the measurement range, reflecting a full separated flow over the wing model. In contrast, for the SJ actuation at 600 Hz and 1000 Hz, the static pressure steadily increases along the chord until about 0.6c, after which it remains high. This indicates the large-portion attachment of the flow was realized under strong actuation. Furthermore, the highest rise in static pressure was observed for the actuation at 1000 Hz.

All above experimental measurements have demonstrated that the highest performance improvement is obtained for the actuation at 1000 Hz. The introduction of the SJ array significantly reduces the strength of uncontrolled large scale vortex structures associated with the

flow separation and enhances the momentum of the boundary layer flow as evidenced from the TR-PIV measurements. The improvement in wing performance is also revealed through increase in lift coefficient, reduction in average drag coefficient, favorable static pressure distribution and FFT power spectra.

4 Conclusions

The primary objective of this paper is to assess the performance enhancement of the wing model using an array of slotted SJs. Experiments were carried out in a subsonic wind-tunnel on a NACA 0025 wing model. The SJ array was operated at various actuation frequencies of 200 Hz, 600 Hz and 1000 Hz and voltage of 200 V. The highest wing performance was observed at an actuation of 1000 Hz resulting in a 35.6% enhancement in lift coefficient and a 33% reduction in average drag coefficient. It is attributed to the substantially high momentum coefficient of 7.8×10^{-4} and high Stokes number of 19.6 that help impart more momentum to the retarding boundary layer flow. It is observed that the actuation at 200 Hz results in negligible performance improvement. The FFT power spectra showed substantial reduction in power spectra for the actuation at 1000 Hz leading to the successful stabilization of the flow-field. These observations are supported by the TR-PIV measurements. For the SJ actuation at 1000 Hz, the TR-PIV measurements showed a substantial reduction in shape factor to below 2.5. The flow separation control mechanism was attributed to the exchange of momentum from outer high energy flow to the inner retarding boundary layer flow and the oscillation of SJ in a certain frequency range affecting the shear layer instability.

References

[1]. Cattafesta, L. N., and Sheplak, M., 2011, "Actuators for active flow control," Annu. Rev. Fluid Mech., 43, pp. 247–272.

[2]. Greenblatt, D., and Wygnanski, I. J., 2000, "The control of flow separation by periodic excitation," Prog. Aerosp. Sci., 36, pp. 487–545.

[3]. Gilarranz, J. L., Traub, L.W., and Rediniotis, O. K., 2005, "A new class of synthetic jet actuator—Part I: design, fabrication and bench top characterization," ASME J. Fluids Eng., 127, pp. 367–376.

[4]. Gilarranz, J. L. Traub, L. W. and Rediniotis, O. K., 2005, "A new class of synthetic jet actuator—Part II: application to flow separation control," ASME J. Fluids Eng., 127, pp. 377–387.

[5]. Jabbal, M., Liddle, S., Potts, J., and Crowther, W., 2013, "Development of design methodology for a synthetic jet actuator array for flow separation control applications," Proc. IMechE. Part G: J. Aerosp. Eng., 227, pp. 110-124.

[6]. Mahalingam, R., and Rumigny, N., 2004, "Thermal management with synthetic jet ejectors," IEEE Trans. Components Packag. Technol., 27, pp. 439–444.

[7]. Lee, C. Y. Y., Woyciekoski, M. L., and Copetti, J. B., 2016, "Experimental study of synthetic jets with rectangular orifice for electronic cooling," Exp. Therm Fluid Sci., 78, pp. 242–248.

[8]. Valiorgue, P., Persoons, T., McGuinn, A., and Murray, D. B., 2009, "Heat transfer mechanisms in an impinging synthetic jet for a small jet-to-surface spacing," Exp. Therm. Fluid Sci., 33, pp. 597–603.

[9]. Rylatt, D. I., and O'Donovan, T. S., 2013, "Heat transfer enhancement to a confined impinging synthetic air jet," Appl. Therm. Eng., 51, pp. 468–475.

[10]. He, W., Luo, Z., Deng, X., Xia, Z., 2019, "Experimental investigation on the performance of a novel dual synthetic jet actuator-based atomization device," International Journal of Heat and Mass Transfer, 142, pp. 118406.

[11]. Gilmore, P., and Sundaresan, V. B., 2017, "Design and analysis of a synthetic jet actuator based fluid atomization device," J. Intell. Mater. Syst. Struct., 28, pp. 2307– 2316.

[12]. Marchitto, L., and Valentino, G., 2017, "Water spray flow characteristics under synthetic jet driven by a piezoelectric actuator," J. Phys. Conf. Ser., 778, pp. 12005.

[13]. Tang, H., Salunkhe, P. B., Zheng, Y., Du, J. and Wu, Y., 2014, "On the use of synthetic jet actuator arrays for active flow separation control," Experimental Thermal and Fluid Science, 57, pp. 1-10.

[14]. Amitay, A., Smith, D. R., Kibens, V., Parekh, D. E., and Glezer, A., 2001, "Aerodynamic flow control over an unconventional airfoil using synthetic jet actuators," AIAA Journal, 39, pp. 361-370.

[15]. Glezer, A., Amitay, M., and Honohan, A. M., 2005, "Aspects of low- and high-frequency actuation for aerodynamic flow control," AIAA Journal, 43, pp. 1501-1514 .

[16]. Franck, J. A., and Colonius, T., 2012, "Effects of actuation frequency on flow control applied to a wall-mounted a hump," Technical Note, AIAA Journal, 50, pp. 1631-1634.

[17]. Timor, I., Hamou, E. B., Guy, Y., and Seifert, A., 2007, Maneuvering aspects and 3D effects of active airfoil flow control," Flow Turbulence Combust, 78, pp. 429-443.

[18]. Sefcovic, J. A., and Smith, D. R., 2010, "Proportional Aerodynamic Control of a Swept Divergent Trailing Edge Wing Using Synthetic Jets," 48th AIAA Aerospace Sciences Meeting, Orlando, Florida, January 4 – 7, 2010.

[19]. Traub, L.W., Miller, A., and Rediniotis, O., 2004, "Effects of synthetic jet actuation on a ramping NACA 0015 airfoil," Journal of Aircraft, 41, pp. 1153-1162.

[20]. Kordik, J., and Travnicek, Z., 2017, "Optimal diameter of nozzles of synthetic jet actuators based on electrodynamic transducers," Experimental Thermal and Fluid Science, 86, pp. 281-294.

[21]. Hong, G., 2006, "Effectiveness of micro synthetic jet actuator enhanced by flow instability in controlling laminar separation caused by adverse pressure gradient," Sensors and Actuators A, 132, pp. 607–615.

[22]. Lee, C., Hong, G., Ha, Q. P., and Mallinson, S. G., 2003, "A piezoelectrically actuated micro synthetic jet for active flow control," Sensors and Actuators A, 108, pp. 168–174.

[23]. Amitay, M., and Glezer, A., 2002, "Role of actuation frequency in controlled flow reattachment over a stalled airfoil," AIAA Journal, 42, pp. 209-216.

[24]. Salunkhe, P. B., Tang, H., Zheng, Y., and Wu, Y., 2016, "PIV measurement of mildly controlled flow over a straight-wing model," International Journal of Heat and Fluid Flow, 62, pp. 552-559.

[25]. Rimasauskiene, R., Matejka, M., Ostachowicz, W., Kurowski, M., Malinowski, P., Wandowski, T., and Rimasauskas, M., 2015, "Experimental research of the synthetic jet generator designs based on actuation of diaphragm with piezoelectric actuator," Mechanical Systems and Signal Processing, 50, pp. 607-614.

[26]. Raben, J., Hariharan, P., Robinson, R., Malinauskas, R., and Vlachos, P., 2014, "Time-resolved particle image velocimetry measurements with wall shear stress and uncertainty quantification for the FDA benchmark nozzle model," Cardiovascular Engineering and Technology, 7, pp. 1-37.

[27]. Moffat, R. J., 1985, "Using uncertainty analysis in the planning of an experiment," Trans. ASME Journal of Fluids Engineering, 107, pp. 173-178.

[28]. Holman, J. P., 1966, Experimental Methods for Engineers, McGraw-Hill Book Company, Tokyo.

[29]. Lazar, E., DeBlauw, B., Glumac, N., Dutton, C., and Elliott, G., 2010, "A Practical Approach to PIV Uncertainty Analysis," 27th AIAA Aerodynamic Measurement Technology and Ground Testing Conference, Chicago, USA, June 28 – July 1, 2010.

[30]. Zhou, J., Tang, H., and Zhong, S., 2009, "Vortex roll-up criterion for synthetic jets," AIAA Journal, 47, pp. 1252–1262.

[31]. Donovan, J. F., Kral, L. D., and Cary, A. W., 1998, "Active flow control applied to an airfoil," 36th AIAA Aerospace Sciences Meeting and Exhibit, Reno, NV, January 12 – 15, 1998.

[32]. Seifert, A., Eliahu, S., Greenblatt, D., and Wygnanski, I., 1998, "Use of piezoelectric actuators for airfoil separation control," Technical Note, AIAA Journal, 36, pp. 1535-1537.

[33]. Lee, H. M., and Wu, Y., 2014, "A Tomo-PIV study of the effects of freestream turbulence on stall delay of the blade of a horizontal-axis wind turbine," Wind Energy, 18, pp. 1185–1205.

LIST OF FIGURE CAPTIONS

a) 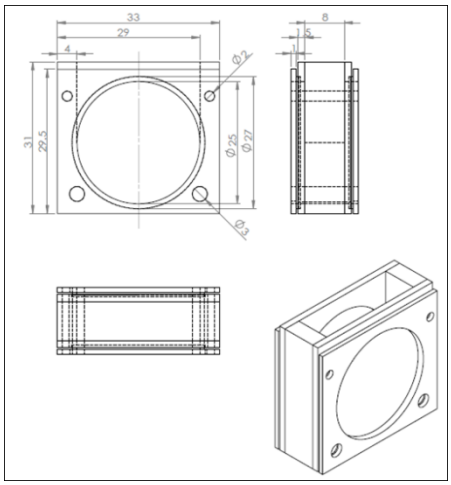

(b) 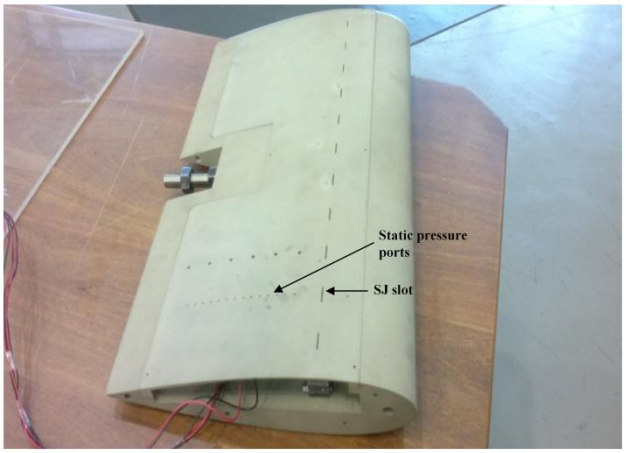

Fig. 1: (a) line drawing of actuator geometry and (b) pictorial view of NACA 0025 wing model

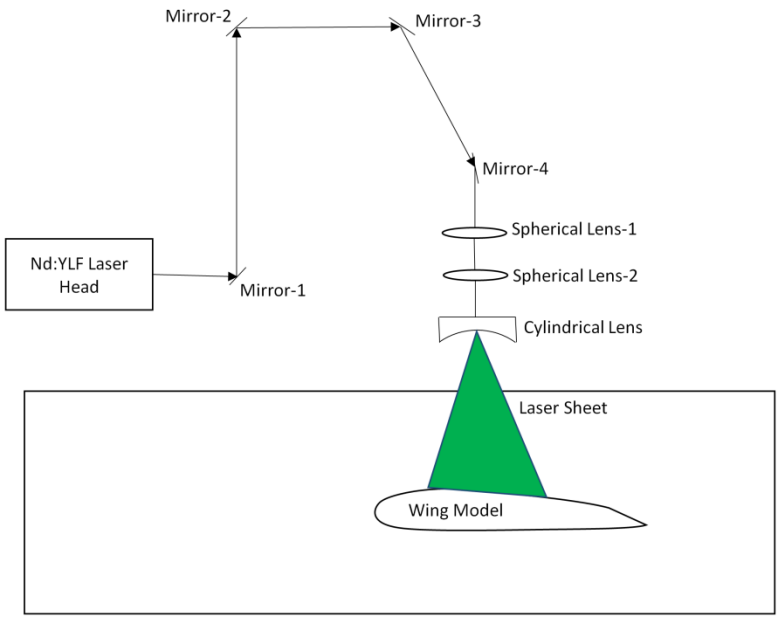

Fig. 2: Schematic representation of TR-PIV system

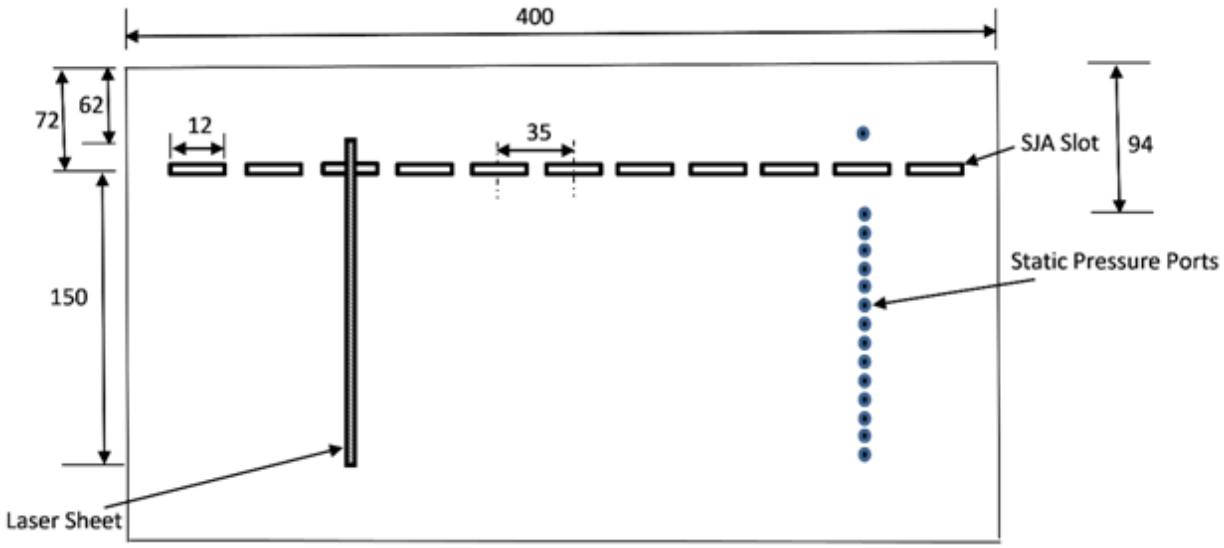

Fig. 3: Location of laser sheet, SJ slots and static pressure ports on a wing model (All dimensions are in mm)

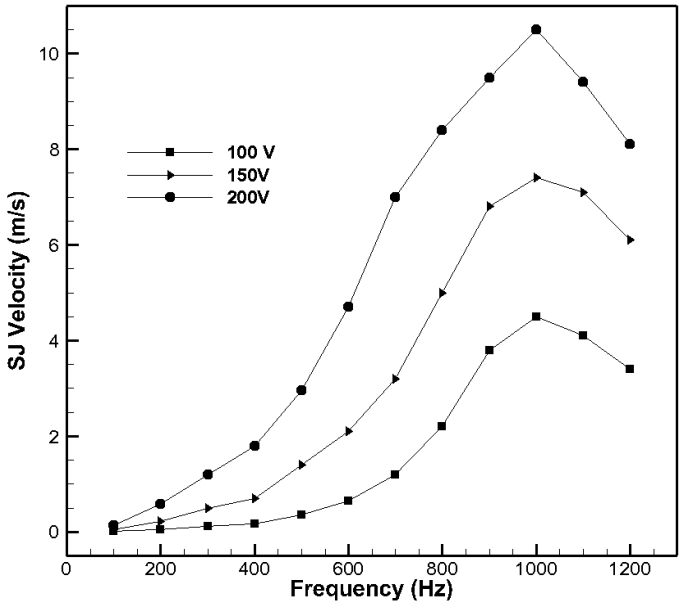

Fig. 4: Variation of SJ velocity against actuation frequencies

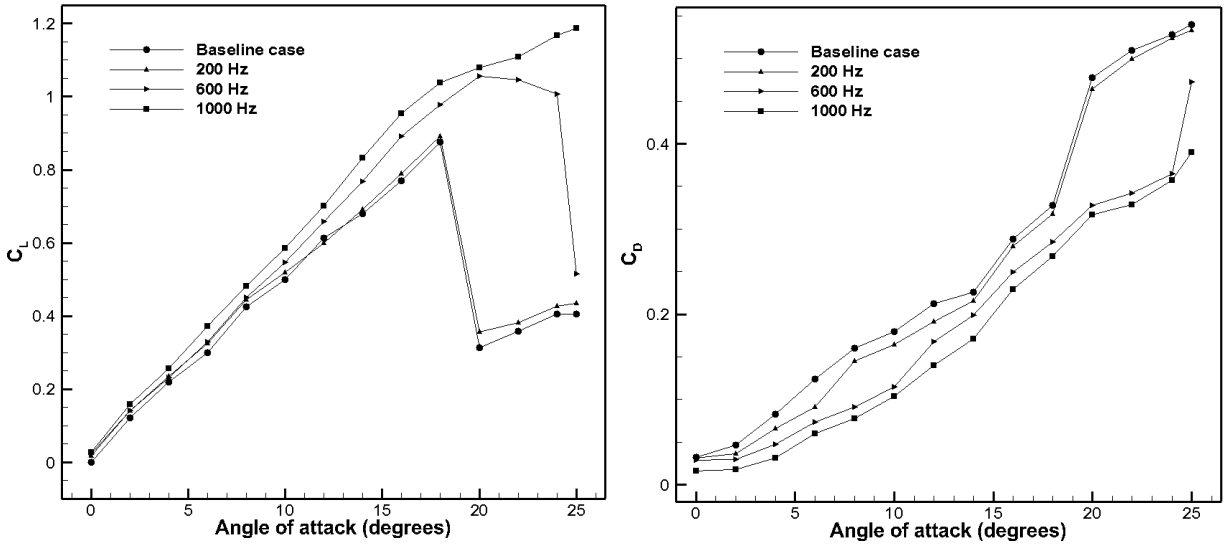

Fig. 5: Variation in (a) lift coefficient and (b) drag coefficient against angles of attack

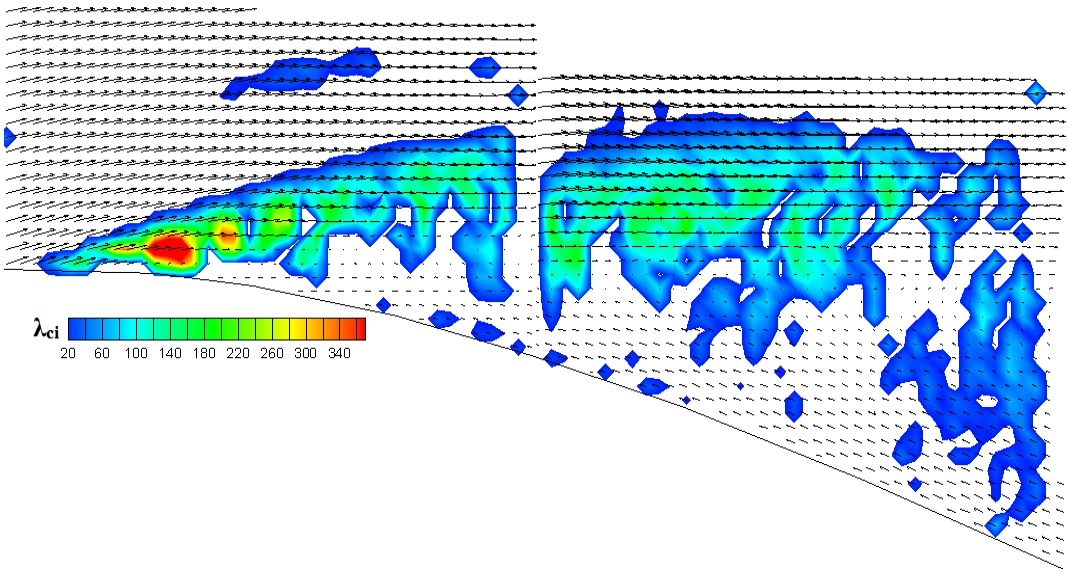

Fig. 6: Time averaged vorticity contours for the baseline case

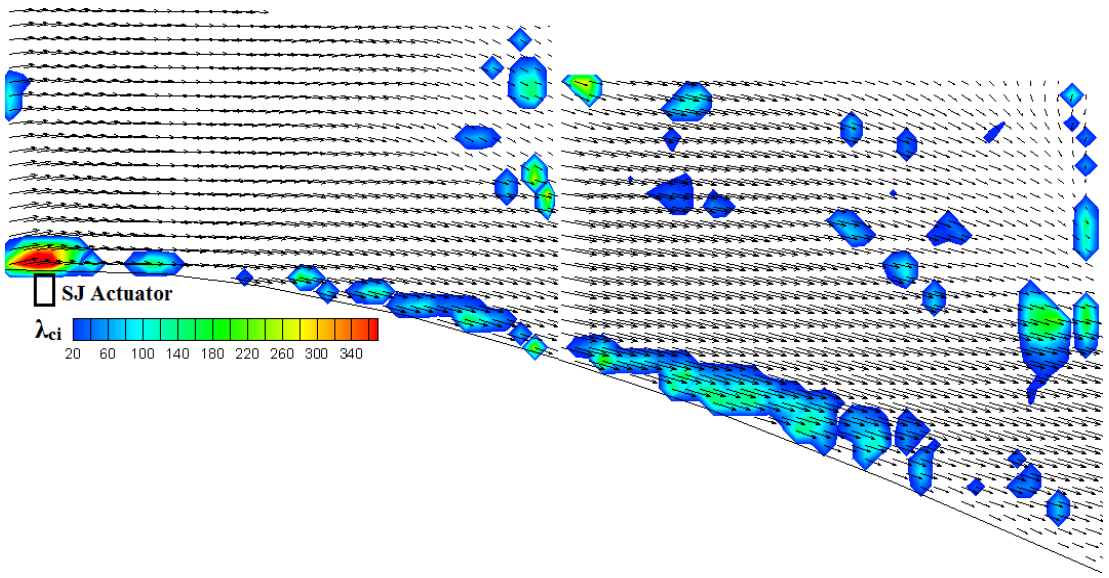

Fig. 7: Time averaged vorticity contours for the SJ actuation at 1000 Hz and 200 V

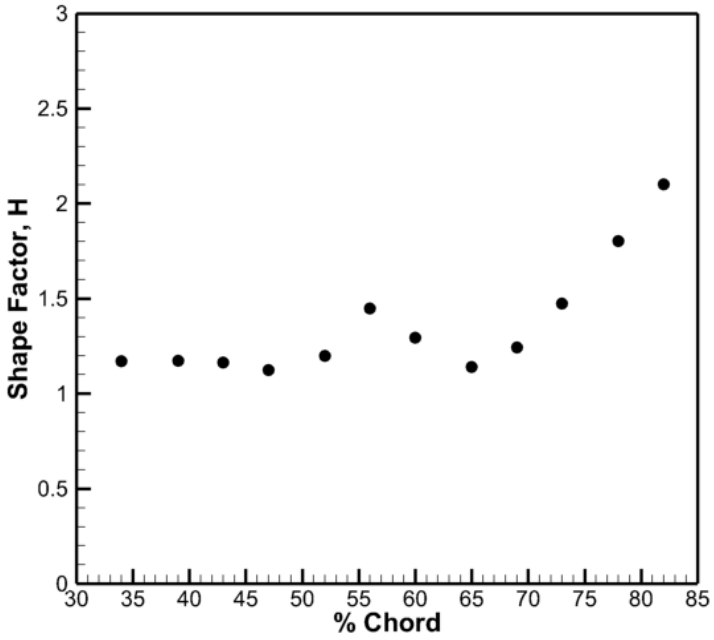

Fig. 8: Variation in shape factor for the SJ actuation case at 1000 Hz and 200 V

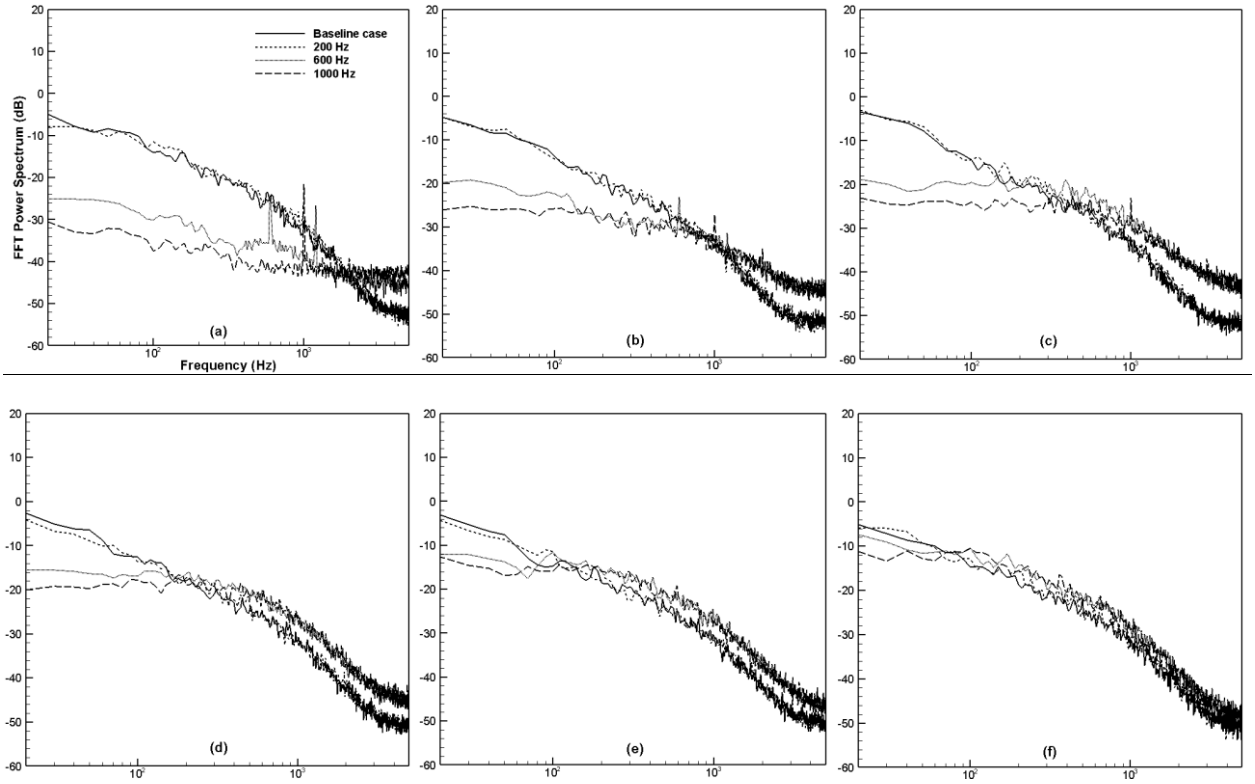

Fig. 9: FFT power spectra for the baseline and SJ actuation at different frequencies along (a) 40% (b) 48% (c) 56% (d) 64% (e) 72% and (f) 80% of the chord

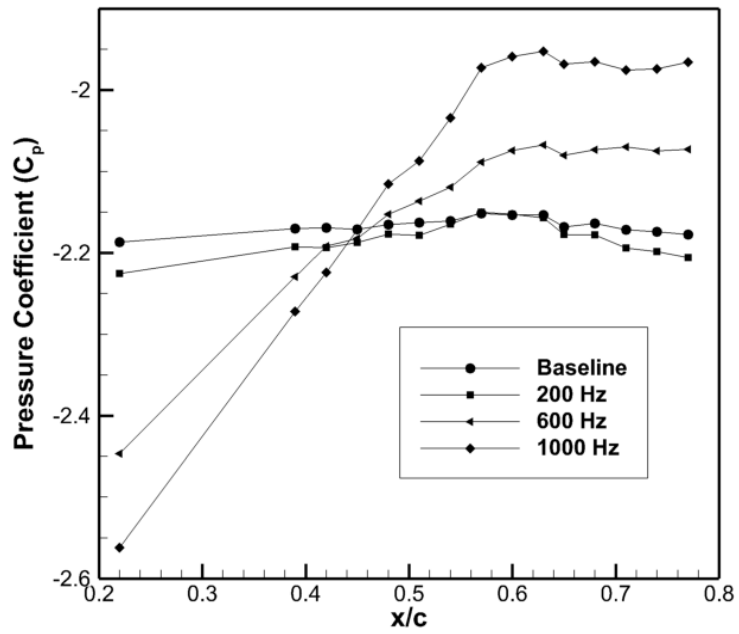

Fig. 10: Static pressure distribution over the wing model